Article

Super-resolution stimulated X-ray Raman spectroscopy

https://doi.org/10.1038/s41586-025-09214-5

Received: 29 January 2025

Accepted: 29 May 2025

Published online: 16 July 2025

Open access

Check for updates

Kai Li[1,2]✉, Christian Ott[3], Marcus Agåker[4,5], Phay J. Ho[2], Gilles Doumy[2], Alexander Magunia[3], Marc Rebholz[3], Marc Simon[6], Tommaso Mazza[7], Alberto De Fanis[7], Thomas M. Baumann[7], Jacobo Montano[7], Nils Rennhack[7], Sergey Usenko[7], Yevheniy Ovcharenko[7], Kalyani Chordiya[8,9], Lan Cheng[10], Jan-Erik Rubensson[4], Michael Meyer[7], Thomas Pfeifer[3]✉, Mette B. Gaarde[9] & Linda Young[1,2,11]✉

Propagation of intense X-ray pulses through dense media has led to the observation of phenomena such as atomic X-ray lasing[1,2], self-induced transparency[3] and stimulated X-ray Raman scattering (SXRS)[4]. SXRS has been long predicted as a means to launch and probe valence-electron wavepackets and as a building block for nonlinear X-ray spectroscopies[5,6]. However, experimental observations of SXRS to date[4,7,8] have not provided spectroscopic information, and theoretical modelling has largely implemented hard-to-realize phase-coherent attosecond pulses. Here we demonstrate SXRS with spectroscopic precision, that is, detection of valence-excited states in neon with a near Fourier-limited joint energy–time resolution of 0.1 eV–40 fs. We used a new covariance analysis between statistically spiky broadband incident X-ray and scattered X-ray Raman pulses. Using 18,000 single shots, we beat not only the incident (about 8 eV) bandwidth but also the approximately 0.2 eV instrumental energy resolution, thus creating super-resolution conditions, in analogy to super-resolved fluorescence microscopy[9]. Our experimental results, supported by ab initio propagation simulations, reveal the competition between lasing in the ion and stimulated Raman scattering in the neutral. We demonstrate enhanced signal collection efficiency and a broad excitation window, surpassing spontaneous Raman efficiencies by orders of magnitude. This stochastic SXRS approach represents a first step towards tracking elementary events that determine chemical outcomes[10].

Controlling the propagation of coherent light pulses through matter underlies many modern laser-based applications. Shortly after the realization of the optical laser in 1960 (ref. 11), researchers discovered that simply propagating intense laser pulses through dense media produced fascinating and useful nonlinear effects, for example, second-harmonic generation[12], stimulated Raman scattering[13] and self-focusing[14]. Stimulated Raman scattering (SRS) with its high conversion efficiency found immediate use as a method not only to generate new laser frequencies by Raman-shifting[15] but also to investigate material properties[16]. SRS applications have advanced hand-in-hand with ultrafast laser technologies—with picosecond pulses enabling studies of vibrational dephasing[17] and with femtosecond pulses shorter than vibrational periods providing a means to induce and detect phase-coherent motions[18] and excited state chemical reactions[19]. The amplification properties of stimulated and spontaneous Raman scattering further enabled the creation of powerful label-free biomedical imaging platforms[20].

The recent revolution in X-ray free-electron lasers (XFELs)[21,22] that can operate in the attosecond–ångstrom regime[23] with pulse energies that far exceed those available from high-harmonic generation sources[24], provides an opportunity to investigate nonlinear propagation phenomena at much shorter wavelengths and time scales[25]. Early XFEL experiments established an understanding of nonlinear X-ray multiphoton processes[26,27], encouraging the long-held goal[28] of extending nonlinear optical spectroscopies to short wavelengths. SXRS is expected to be exceptionally versatile, as quasi-atomic core-level resonances imply picometre spatial resolution in addition to the temporal resolution. Conceptual investigations using phase-coherent attosecond X-ray pulse pairs have targeted, for example, energy transfer in large molecules and concerted electron and nuclear dynamics near conical intersections[10]. SXRS, similar to spontaneous X-ray Raman scattering[29], produces spectral features narrower than the lifetime width of the intermediate core-hole state, in contrast to traditional linear X-ray absorption (XAS) and emission (XES) spectroscopies. Furthermore, SXRS provides a large directional signal enhancement (10^8) relative to spontaneous X-ray Raman scattering[4].

These attributes position SXRS as an essential building block for nonlinear X-ray spectroscopy[6] and steps towards its realization as a spectroscopic tool using existing SASE XFEL sources have been made.

[1]Department of Physics, The University of Chicago, Chicago, IL, USA. [2]Chemical Sciences and Engineering Division, Argonne National Laboratory, Lemont, IL, USA. [3]Max-Planck-Institut für Kernphysik, Heidelberg, Germany. [4]Department of Physics and Astronomy, Uppsala University, Uppsala, Sweden. [5]MAX IV Laboratory, Lund University, Lund, Sweden. [6]Laboratoire de Chimie Physique-Matière et Rayonnement, Sorbonne Université, CNRS, Paris, France. [7]European XFEL, Schenefeld, Germany. [8]Department of Physics, University of Hamburg, Hamburg, Germany. [9]Department of Physics and Astronomy, Louisiana State University, Baton Rouge, LA, USA. [10]Department of Chemistry, Johns Hopkins University, Baltimore, MD, USA. [11]James Franck Institute, The University of Chicago, Chicago, IL, USA. ✉e-mail: kail@uchicago.edu; thomas.pfeifer@mpi-hd.mpg.de; young@anl.gov

Directional amplification of SXRS was initially observed by propagating a SASE pulse, consisting of a chaotic ensemble of attosecond temporal spikes within an approximately 40 fs envelope, through a dense neon gas target[4,30]. The gain mechanism, amplified spontaneous emission (ASE), was identified in the seminal study that produced the neon Kα X-ray laser (XRL)[1]. Despite extensive investigations of ASE in the hard X-ray regime as a time-resolved spectroscopic tool in Mn solutions[31], resolving the chemically important sub-eV multiplet valence electronic structure is yet to be realized[32]. In the isolated-system limit, that is, without amplification, the SXRS transfer efficiency to valence-excited states was investigated with SASE pulses using a new photon-recoil imaging detection method[8] and with attosecond pulses in a molecule[7]; both finding good agreement with theoretical calculations. However, in neither case were the targeted valence-excited states spectroscopically distinguished, the observed features being limited by the 8-eV (5-eV) spectral bandwidth of the SASE (attosecond) pulse.

Here we establish stochastic stimulated X-ray Raman scattering (s-SXRS) as a spectroscopic tool—harnessing exponential signal amplification and using covariance analysis to produce 0.1 eV–40 fs resolution Raman snapshots covering the entire incident SASE bandwidth. Noise, in the form of stochastically fluctuating intensity spikes in both the temporal and spectral domains[33], becomes an asset in this technique. The temporal spikes have attosecond durations inversely proportional to the SASE gain bandwidth, $\sigma_\omega \approx 7.5$ eV. The spectral spikes have widths inversely proportional to the bunch duration, $\omega_{coh} = h/T_b \approx 0.1$ eV (for $T_b = 40$ fs) (ref. 34). In the s-SXRS covariance analysis[35], we correlate fluctuations on a shot-by-shot basis between the incident and Raman scattered beams. Thus, the resolution is limited by the individual spikes that are measured[30,36]. By further introducing a super-resolution approach to covariance analysis, we eliminate instrumental broadening and reach pixel-limited resolution. This results in an 80-fold improved spectral resolution over the incident linewidth—exceeding the improvement in previous XAS and XES studies that exploited correlations in SASE X-ray pulses, but where resolution is intrinsically limited by the intermediate state lifetime[37,38]. Because the entire SASE bandwidth contributes simultaneously and the Raman signal is directionally amplified, data collection was rapid, suggesting that the combination of high-repetition-rate sources and detectors could improve measurement access and accuracy in more complex systems[10].

Stochastic stimulated X-ray Raman scattering

The layout of the s-SXRS experimental setup is shown in Fig. 1a. An incident SASE XFEL pulse (7.5 eV full width at half-maximum (FWHM), 40 fs) from the European XFEL was focused into a gas cell containing 1–4 bar neon with the central photon energy resonant with the $1s \rightarrow 3p$ transition in neon. The output was attenuated by Al filters and spatially constrained by a slit before being spectrally dispersed on a two-dimensional (2D) detector. A typical single-shot spectrum recorded consisted of stimulated emission photons (XRL + XRS) at lower energy $\omega_2 \approx 849$ eV and the transmitted incident photons at higher energy $\omega_1 \approx 867$ eV.

The principle of s-SXRS is shown in Fig. 1b. The incident SASE pulse contains random spectral spikes over a bandwidth that covers the neutral core-excited Rydberg states and continuum. Photons with energy higher than the ionization threshold induce X-ray emission at constant photon energy, that is, the XRL, with the excess energy carried away by the photoelectron. Photons with energy below the ionization threshold induce Raman transitions through core excitation, followed by Raman photon emission channels. Energy conservation requires the photon energy loss to equal the excited state energies of the neutral atom. Thus, the emitted Raman photon energy, ω_2, disperses with the incident photon energy, ω_1. This energy correlation between incident SASE spikes and the Raman emission peaks generates a correlation along the dispersive line $\omega_2 = \omega_1 - \Delta\omega$ for each Raman channel, where $\Delta\omega$ is the excited state energy of the neutral atom. The exponential amplification of the spontaneous Raman seed greatly increases the photon yields and enables the measurement of single-shot Raman spectra. The results of many SASE shots with random spikes serve as input to the covariance analysis.

Amplification of stimulated X-ray Raman scattering

The dependence of the total stimulated emission pulse energy (XRL + XRS) on the incident SASE pulse energy is shown in Fig. 2. Owing to the high intensity of the incident SASE pulse, up to 4×10^{18} W cm^{-2}, a population inversion is propagated with the pulse through the dense neon gas target at 2 bar. The incident SASE pulse energy was controlled by a gas attenuator and measured by a gas monitor detector. The peak intensity of the incident pulse was calculated assuming a beam focal diameter of 2 μm (FWHM), a pulse duration of 40 fs and a spike-to-average intensity ratio of about 2 as measured. The averaged emission spectrum contains both XRS and XRL components (Fig. 2, inset). The XRS and XRL components can be separated by peak fitting; the XRL bandwidth is found to be 0.29 eV (FWHM) at the highest intensity. With the incident photon energy centred on resonance at 867.5 eV, the emission pulse energy is dominated by broadband XRS, which contains scattering from all SASE spikes. The XRL contribution to the total emission yield (purple-dashed line) increases at lower incident intensities because of the larger transition dipole for the ion (XRL) compared with the neutral (XRS). An absolute conversion efficiency from SASE to stimulated emission (XRL + XRS) of a few per cent was measured.

To gain insight into the stimulated emission from the SASE pulse, isolated attosecond pulse (IAP) propagation simulations were conducted by solving the coupled time-dependent Schrödinger and Maxwell wave equations[25]. A Gaussian IAP with a bandwidth of 7.5 eV (FWHM), comparable to the measured average SASE bandwidth, has a transform-limited pulse duration of about 0.25 fs, representative of a single temporal spike in the SASE pulse. Simulations of propagation of a Gaussian IAP yield a pulse energy amplification curve that parallels the experimental SASE pulse results as shown in Fig. 2. This suggests that XRS yield from the SASE pulse equals that of a collection of many short Gaussian pulses. This is also supported by the ratio of around 30 between emission yields for SASE compared with IAP, consistent with the number of spikes found in a typical SASE pulse.

Covariance analysis for high-resolution s-SXRS maps

Before describing super-resolution covariance, we first analyse our data in terms of the established covariance method[35]. We use the spectral intensity covariance of the stochastically fluctuating incident and scattered SASE XFEL pulses to obtain an effective cross-section for SXRS. The spectral intensity covariance is defined as $\mathrm{cov}(I_1, I_2) = \langle I(\omega_1)I(\omega_2)\rangle - \langle I(\omega_1)\rangle\langle I(\omega_2)\rangle$ between the transmitted incident $I_1 = I(\omega_1)$ and the emission $I_2 = I(\omega_2)$ where $\langle\rangle$ indicates the ensemble average over SASE shots. We find that the covariance $\mathrm{cov}(I_1, I_2) = \sigma_{\mathrm{eff}}\langle I_1\rangle$ is related to the effective cross-section $\sigma_{\mathrm{eff}} = I_2/I_0$, where I_0 is the incident spectrum (see Supplementary Information section I-A). In practice, to remove false correlations introduced by pulse-energy fluctuations, we calculate the partial covariance normalized to the average transmitted incident spectrum[39]:

$$\frac{\mathrm{pcov}(I_1, I_2; E)}{\langle I_1\rangle} = \frac{\mathrm{cov}(I_1, I_2) - \mathrm{cov}(I_1, E)\mathrm{cov}(I_2, E)/\mathrm{var}(E)}{\langle I_1\rangle} \propto \sigma_{\mathrm{eff}} \qquad (1)$$

where E is the pulse energy proportional to the integral of the transmitted incident spectra. This partial covariance also gives results proportional to the effective stimulated Raman scattering cross-section. Various covariance normalizations can be used to obtain results with different physical meanings.

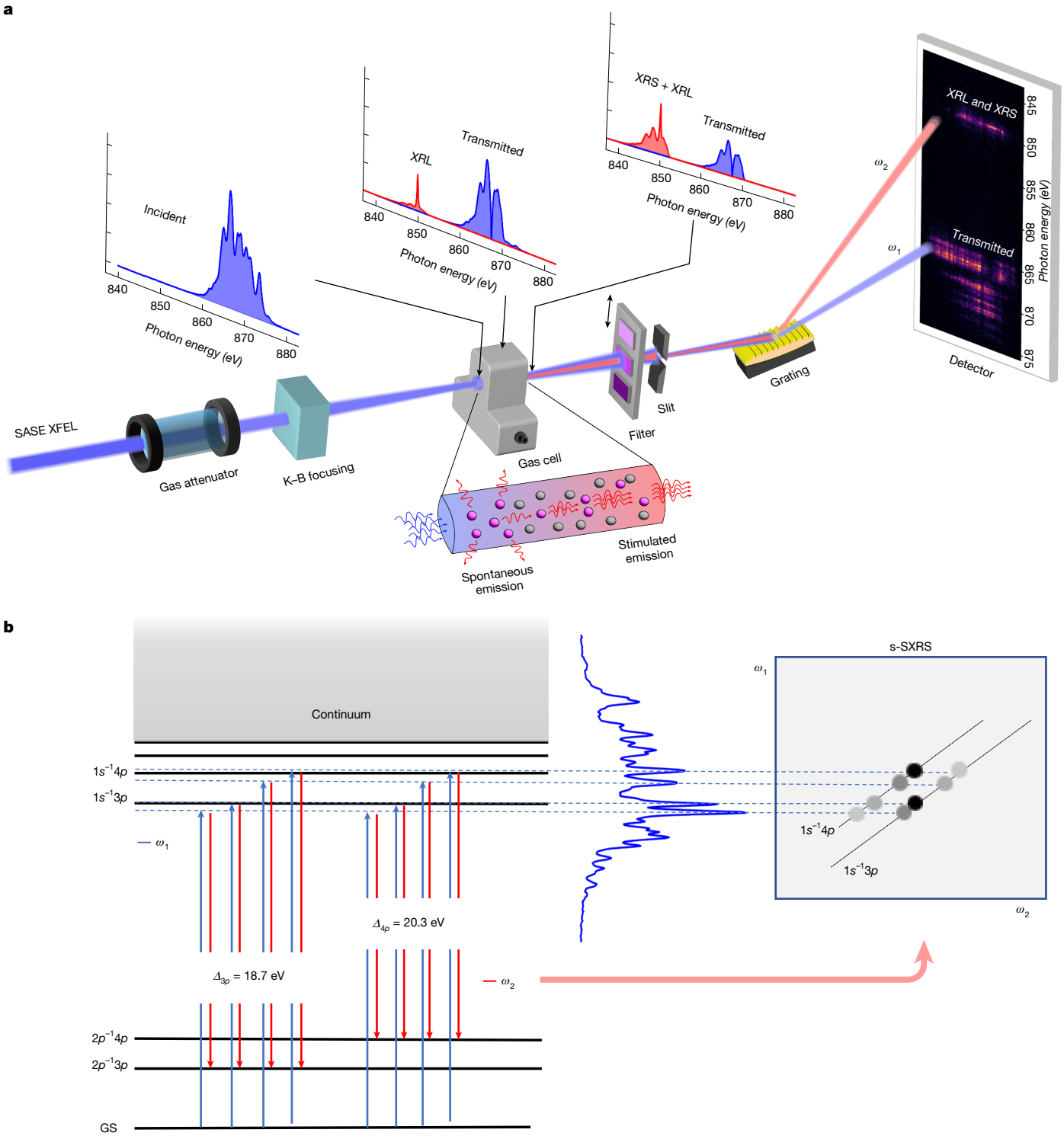

Fig. 1 | s-SXRS experimental layout and concept. a, A SASE XFEL beam is focused onto a 4.5-mm gas cell filled with neon. The incident X-ray intensity was controlled by a gas attenuator, and the transmitted X-ray beam was attenuated by Al filters with thicknesses 3.5 µm, 5 µm and 10 µm. A slit constrained the size of the transmitted X-ray beam before the spectrum was measured by dispersing the beam on a 2D detector. **b**, Level scheme for stimulated X-ray Raman transitions. The incident SASE X-ray (in blue) produces core-excited states ($1s^{-1}3p$, $1s^{-1}4p$), which transition to final states ($2p^{-1}3p$, $2p^{-1}4p$) by emission of Raman photons. Each spectral spike in the SASE pulse introduces a corresponding Raman transition, and covariance analysis of a collection of single-shot Raman scattering spectra (ω_2) with the transmitted incident spectra (ω_1) generates dispersive lines indicative of the constant energy loss of Raman transitions through different channels.

The experimental s-SXRS maps with different gas pressure and photon energy are shown in Fig. 3a. Each panel uses 18,000 single-shot spectra, acquired in about 30 min at a 10-Hz XFEL repetition rate limited by detector readout time. At 1-bar pressure with the incident photon energy centred at 867.5 eV, a combination of 3*p*, 4*p* s-SXRS and XRL signals are observed (Fig. 3a, left). The s-SXRS signals disperse with the incident photon energy and thus appear as diagonal lines, most clearly for the 3*p*. The expected constant-energy-loss lines associated

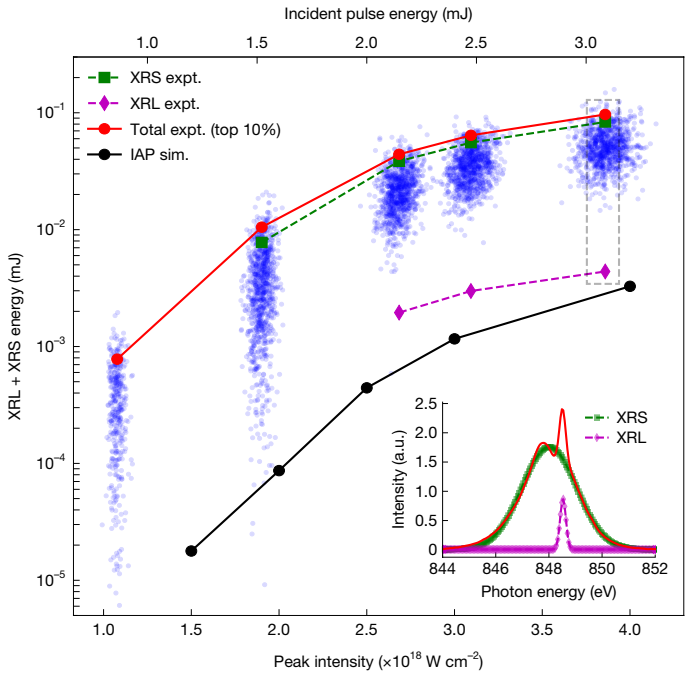

Fig. 2 | Dependence of stimulated emission pulse energy (XRL + XRS) on incident SASE pulse energy. The incident SASE intensity is changed by the gas attenuator (GATT) to produce transmissions of 25%, 50%, 70%, 80% and 100%. The results of 1,000 shots (blue dots) for each transmission value fluctuate because of the randomness of the single-shot SASE energy spectrum—SXRS gain occurs when a SASE spike matches a transition energy as shown in Fig. 1b. SASE pulses at the lowest peak intensity generate emission spectra with signals that barely emerge from the detector noise, setting the limit for discrimination of XRL and XRS. The average emission pulse energy of the top 10% shots (red) increases exponentially before saturation. The stimulated emission has two components: XRL (magenta) and XRS (green). The inset shows the decomposition of the XRL and XRS yield for the highest intensity data obtained by averaging the individual shots. Simulations of isolated attosecond pulse propagation using a 0.25-fs Gaussian pulse with 7.5 eV bandwidth (black) as a function of peak intensity parallel the experimentally observed gain with SASE pulses (red).

with Raman transitions from different Rydberg states are represented by the diagonal dashed lines, and the dashed horizontal lines indicate the energies of the neutral Ne Rydberg states[40]. These results resemble traditional spontaneous X-ray Raman scattering, which is obtained by measuring the emission with high resolution while scanning incident monochromatic X-ray radiation[41].

At a higher gas pressure, 1.5 bar (Fig. 3a, middle), in which propagation effects become more notable, the amplification of off-resonant scattering leads to an extension of the 3*p* s-SXRS signal along the dispersive line. The strong absorption of incident photons removes the intensity of the transmitted incident ω_1 at resonances, resulting in a horizontal background and interruption of the 3*p* s-SXRS. With the gas pressure at 2 bar and incident photon energy centred at slightly higher energy, 870 eV (Fig. 3a, right), Raman scattering signals involving higher Rydberg states are accentuated, as seen in the inset. A hole near the $1s \rightarrow 3p$ resonance develops in the dispersive Raman line (along the diagonal) as the pressure is increased. Figure 3b shows that this feature is reproduced in the large-scale simulations, as described below and shown in more detail in Supplementary Fig. 2. The broadened line shape with a hole is characteristic of propagation-driven temporal reshaping in combination with a phase-dressed absorption or emission feature, similar to what happens in Rabi cycling or strong-field dressing[42]. In our case, we speculate that this occurs when the sub-pulses of the incident light, generated by the strong $1s \rightarrow 3p$ transition, give rise to phase-shifted SXRS emission. The s-SXRS from a single run covers a spectral range close to the bandwidth of the SASE ~ 7.5 eV. To form an s-SXRS map that covers a larger energy range, the runs with different central photon energies can be combined—that is, single shots from individual runs are added to be single shots in a combined SXRS—and then the covariance of the combined single shots can be calculated by equation (1).

We simulated the s-SXRS maps using SASE pulses generated by the partial-coherence method[43,44], with an average pulse duration of 40 fs and bandwidth of 7.5 eV (Fig. 3b). The generated SASE pulses reproduce well the number of spikes observed (Methods). Simulations of 4,096 SASE shots propagating through neon gas were carried out on the THETA supercomputer at Argonne National Laboratory. Theoretical simulations, including the 3*p* and 4*p* Rydberg states in neutral Ne with different gas pressures, are in good agreement with experimental data as shown in Fig. 3a,b—even with the simplified energy level structure used. The lack of higher-lying Rydberg states in the calculation (to conserve computation time) leads to a stronger dispersive behaviour of the 4*p* s-SXRS than in the experiment, and a corresponding lack of *np* peaks along the vertical dashed line. In contrast to spontaneous Raman scattering, in which the lineshape along the dispersive direction is a Lorentzian profile with a maximum centred at the resonance and in which the signal width depends on the intermediate excited state lifetime, the s-SXRS signal extends farther along the dispersive line as the gas pressure increases, as shown both experimentally and theoretically in Fig. 3. Besides confirming the experimental observations, our simulations provide valuable insights on how to emphasize different signals in s-SXRS and how to eliminate the noise and background by incorporating methods measuring the incident spectrum[45] (Supplementary Information section I-B).

We observe propagation phenomena and also extract the instrumental resolution from the s-SXRS maps. Transient gain narrowing for SXRS was detected by changing the target thickness to access the exponential and saturation regimes. The FWHM linewidth first decreased from 0.42 eV to 0.28 eV for gas pressures from 1.0 bar to 2.0 bar and then increased to 0.32 eV at 4 bar. This transient gain narrowing in SXRS was reproduced by our simulation, and parallels those predicted for the XRL[46] (Supplementary Information section III-B). To extract the instrumental resolution, we assume the spectrometer resolution function and SASE spikes to be Gaussian. The covariance linewidth can be calculated by $\sqrt{\frac{1}{2\,\sigma_t^2} + 2\,\sigma_s^2}$, where σ_t is the FWHM SASE pulse duration and σ_s is the FWHM spectrometer resolution[47]. For $\sigma_t = 40$ fs and $\sigma_s = 0.18$ eV in our experiment, the covariance linewidth of the s-SXRS is calculated to be 0.26 eV, comparable to the lowest measured resolution of 0.28 eV. We note that the instrumental resolution obtained from the covariance map matches that which we measured independently from the absorption profile of the $1s \rightarrow 3p$ resonance in neutral neon at low XFEL intensity and low target density; the lineshape was fitted as a Voigt profile with Lorentzian and Gaussian components of 0.27 eV and 0.18 eV, respectively. This analysis shows that the s-SXRS spectral width is almost entirely determined by the spectrometer resolution. Instrumental improvements would imply considerable effort. In the quest for improved resolution in spontaneous XRS experiments, large, advanced instruments have been conceived and constructed[48].

To overcome the limitation of spectrometer resolution, we introduce a super-resolution s-SXRS method shown in Fig. 4. Here, a peak finding algorithm identifies the peaks of the Raman and transmitted incident SASE single-shot spectra and only the peak values are selected to form a super-resolution s-SXRS map. Each red dot in Fig. 4a represents a single detector pixel in the dispersive direction. The peak position can be found with much better precision than the bandwidth of the measured SASE spikes, in direct analogy with super-resolution fluorescence microscopy[9,49]. Thus, the normalized partial covariance map with super-resolution spectra improves the resolution to about 0.1 eV (see

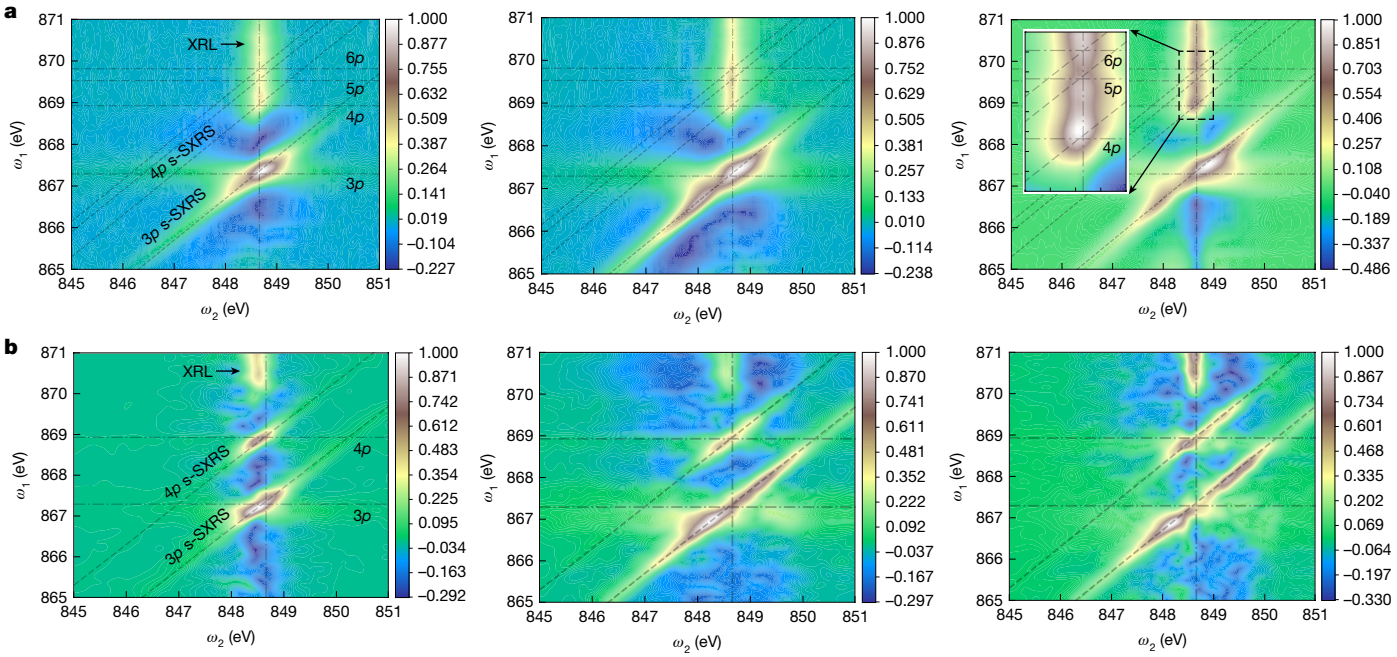

Fig. 3 | Experimental and simulated s-SXRS. a, Experimental s-SXRS maps at 1 bar, 1.5 bar and 2 bar gas pressure. At 1 bar gas pressure on resonance (867.5 eV), the map shows 3*p* and 4*p* Raman signals as well as XRL. At 1.5 bar, the s-SXRS signal extends farther along the constant energy loss line. Strong resonant absorption by the $1s \rightarrow 3p$ transition at 867.5 eV leaves almost no transmitted signal, causing a horizontal background feature after partial covariance normalization. At 2 bar pressure with incident X-ray photon energy slightly above resonance (870 eV), Raman transitions from the Rydberg states (4*p*, 5*p*, 6*p*) are accentuated. **b**, s-SXRS simulations with seven states, including the $1s^{-1}3p$ and $1s^{-1}4p$ core-excited Rydberg states and their corresponding valence-excited multiplet states for the experimental conditions in **a**.

Supplementary Information section I-C). The super-resolution s-SXRS map with 1 bar and 867.5 eV photon energy distinguishes dispersive lines from the individual valence-excited states, $2p^{-1}3p\,{}^1S_0$ and ${}^1D_2$ split by 0.31 eV, achieving the goal of femtosecond X-ray snapshots of sub-eV separated valence-excited states[32].

Discussion and summary

Nonlinear two-photon s-SXRS provides advantages over spontaneous resonant inelastic scattering (RIXS). s-SXRS is more selective than spontaneous Raman scattering—simply by means of having control over the two photons involved. For our case (Fig. 4c), pure linear polarization stimulated Raman emission (red solid lines) populates only the valence-excited ${}^1S_0$ and ${}^1D_2$ states, in contrast to spontaneous Raman (black dashed lines). The populated valence-excited states can be easily visualized on an energy-loss scale, obtained by rotating the 2D-covariance map by 45° and projecting onto the $(\omega_1 - \omega_2)$ axis. Figure 4b compares experimental s-SXRS spectra with simulated spectra on the energy-loss axis. The top panel shows experimental s-SXRS energy-loss spectra obtained with (red solid) and without (red dashed line) the super-resolution s-SXRS method applied. The super-resolution method reproduces the more intense ${}^1D_2$ and weaker ${}^1S_0$ valence-excited states predicted by simulation using an ideal spectrometer resolution (blue solid line). The agreement between simulation and experiment is notable, in both excitation energy and intensity. After convolution with the spectrometer resolution (blue dashed line), the simulated energy-loss spectrum matches the direct covariance s-SXRS result (red dashed line) and fails to distinguish the valence-excited states. Traditional s-SXRS spectral resolution is limited by both the SASE spike width and spectrometer instrumental broadening, whereas the super-resolution s-SXRS is limited by the peak localization uncertainty. In our study, the peak localization precision is primarily limited by the detector pixel size (Methods). Thus, the super-resolution s-SXRS method can overcome both spectrometer and SASE spike bandwidth broadening, and with a smaller detector pixel size or extended measurement geometry, this effect would be pronounced.

In summary, our study of nonlinear propagation of intense SASE X-ray pulses through dense neon gas has demonstrated valence-state-resolved core-level SXRS with joint temporal–spectral resolution of 40 fs and 0.1 eV. This, s-SXRS was accomplished using fluctuations in SASE spike structure combined with propagation-based Raman amplification to provide snapshots from a broadband SASE pulse with narrowband-spike spectral resolution on a shot-by-shot basis. The directional enhancement (approximately 10^8) of the Raman signal allows rapid parallelized data acquisition. The super-resolution covariance method introduced here essentially eliminates instrumental broadening—going hand-in-hand with the elimination of core-hole lifetime broadening inherent in X-ray Raman processes. The super-resolution covariance is analogous to super-resolved fluorescence microscopy in which features are localized to better than the diffraction limit, and the obtained localization is inversely proportional to the square root of the number of photons detected[49]. With this new technique, we resolved separate X-ray Raman signals associated with sub-eV split valence-excited states. There are obvious avenues to improve the present configuration, which used a short grating-to-detector distance resulting in a pixel-limited super-resolution and a limited 10-Hz detector readout speed.

Looking towards the future, we may predict extending the present demonstration of s-SXRS on atoms not only to gas phase molecular systems such as CO (ref. 36), to examine feasibility in systems with additional degrees of freedom, but also to applications in condensed phases. The recent observation of SXRS in condensed phase[50] suggests that s-SXRS might be applicable, assuming that raster scanning to assure a pristine sample for each X-ray shot is achievable. Although the present work focused on energy-domain spectroscopy, the increased predictive power of our TDSE/MWE code suggests that propagation of isolated attosecond pulses[23] through resonant media may be explored to reshape pulses while maintaining phase coherence. These tailored

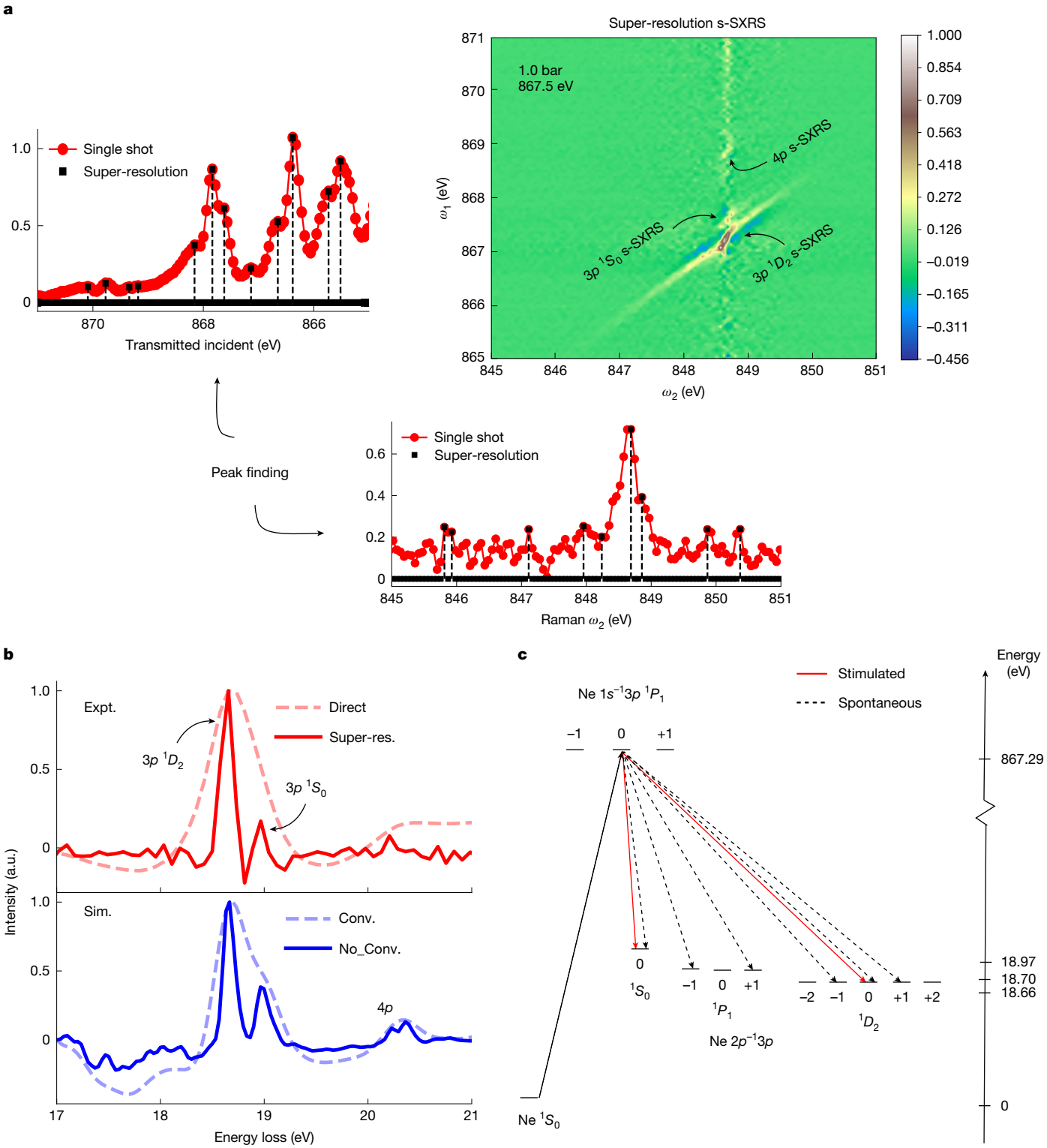

Fig. 4 | Super-resolution s-SXRS. a, A random single-shot spectrum (red dots) with peaks selected by the peak-finder code (black dots) for the transmitted incident (left) and scattered Raman (bottom). The super-resolution s-SXRS map (1 bar at 867.5 eV central energy) can be compared with the spectrum shown in Fig. 3a (left). The super-resolution s-SXRS map reduces backgrounds and improves resolution to around 0.1 eV, to reveal both the $2p^{-1}3p\,^1S_0$ and $^1D_2$ dispersive lines. **b**, s-SXRS spectra plotted on the energy-loss axis. Top, experimental s-SXRS (1 bar at 867.5 eV) with directly measured s-SXRS (red dashed) and super-resolution s-SXRS (red solid). Bottom, simulated s-SXRS with ideal spectrometer resolution (blue solid) and convolved with experimental 0.18 eV spectrometer resolution (blue dashed). Super-resolution s-SXRS removes instrumental broadening and reproduces the simulated s-SXRS with ideal spectrometer resolution. **c**, States involved in spontaneous and stimulated Raman transitions. Spontaneous Raman (black dashed) transitions occur to all multiplet components, whereas the stimulated Raman transitions with linearly polarized X-rays (red solid) select only the $^1S_0$ and $^1D_2$ states.

pulses could be useful for attosecond impulsive stimulated Raman spectroscopy as recently observed in liquid water[51]. Here, by exploiting inherent statistical fluctuations, our work represents a key step towards nonlinear X-ray spectroscopies using readily obtainable SASE pulses from XFELs to eventually study site-specific, valence-excited state dynamics, a long-standing goal in chemistry[52].

Online content

Any methods, additional references, Nature Portfolio reporting summaries, source data, extended data, supplementary information, acknowledgements, peer review information; details of author contributions and competing interests; and statements of data and code availability are available at https://doi.org/10.1038/s41586-025-09214-5.

1. Rohringer, N. et al. Atomic inner-shell X-ray laser at 1.46 nanometres pumped by an X-ray free-electron laser. *Nature* **481**, 488–491 (2012).
2. Yoneda, H. et al. Atomic inner-shell laser at 1.5-ångström wavelength pumped by an X-ray free-electron laser. *Nature* **524**, 446–449 (2015).
3. Chen, Z. et al. Ultrafast self-induced X-ray transparency and loss of magnetic diffraction. *Phys. Rev. Lett.* **121**, 137403 (2018).
4. Weninger, C. et al. Stimulated electronic X-ray Raman scattering. *Phys. Rev. Lett.* **111**, 233902 (2013).
5. Mukamel, S., Healion, D., Zhang, Y. & Biggs, J. D. Multidimensional attosecond resonant X-ray spectroscopy of molecules: lessons from the optical regime. *Annu. Rev. Phys. Chem.* **64**, 101–127 (2013).
6. Rohringer, N. X-ray Raman scattering: a building block for nonlinear spectroscopy. *Philos. Trans. R. Soc. A* **377**, 20170471 (2019).
7. O'Neal, J. T. et al. Electronic population transfer via impulsive stimulated X-ray Raman scattering with attosecond soft-X-ray pulses. *Phys. Rev. Lett.* **125**, 073203 (2020).
8. Eichmann, U. et al. Photon-recoil imaging: expanding the view of nonlinear X-ray physics. *Science* **369**, 1630–1633 (2020).
9. Möckl, L., Lamb, D. C. & Bräuchle, C. Super-resolved fluorescence microscopy: Nobel Prize in Chemistry 2014 for Eric Betzig, Stefan Hell, and William E. Moerner. *Angew. Chem. Int. Ed.* **53**, 13972–13977 (2014).
10. Keefer, D. et al. Ultrafast X-ray probes of elementary molecular events. *Annu. Rev. Phys. Chem.* **74**, 73–97 (2023).
11. Maiman, T. H. Stimulated optical radiation in ruby. *Nature* **187**, 493–494 (1960).
12. Franken, P. A., Hill, A. E., Peters, C. W. & Weinreich, G. Generation of optical harmonics. *Phys. Rev. Lett.* **7**, 118–119 (1961).
13. Shen, Y. R. & Bloembergen, N. Theory of stimulated Brillouin and Raman scattering. *Phys. Rev.* **137**, A1787–A1805 (1965).
14. Kelley, P. L. Self-focusing of optical beams. *Phys. Rev. Lett.* **15**, 1005–1008 (1965).
15. Minck, R., Terhune, R. & Rado, W. Laser-stimulated Raman effect and resonant four-photon interactions in gases H2, D2, and CH4. *Appl. Phys. Lett.* **3**, 181–184 (1963).
16. Giordmaine, J. A. & Kaiser, W. Light scattering by coherently driven lattice vibrations. *Phys. Rev.* **144**, 676–688 (1966).
17. Von der Linde, D., Laubereau, A. & Kaiser, W. Molecular vibrations in liquids: direct measurement of the molecular dephasing time; determination of the shape of picosecond light pulses. *Phys. Rev. Lett.* **26**, 954–957 (1971).
18. Dhar, L., Rogers, J. A. & Nelson, K. A. Time-resolved vibrational spectroscopy in the impulsive limit. *Chem. Rev.* **94**, 157–193 (1994).
19. Kukura, P., McCamant, D. W. & Mathies, R. A. Femtosecond stimulated Raman spectroscopy. *Annu. Rev. Phys. Chem.* **58**, 461–488 (2007).
20. Saar, B. G. et al. Video-rate molecular imaging in vivo with stimulated Raman scattering. *Science* **330**, 1368–1370 (2010).
21. Emma, P. et al. First lasing and operation of an ångstrom-wavelength free-electron laser. *Nat. Photon.* **4**, 641–647 (2010).
22. Decking, W. et al. A MHz-repetition-rate hard X-ray free-electron laser driven by a superconducting linear accelerator. *Nat. Photon.* **14**, 391–397 (2020).
23. Duris, J. et al. Tunable isolated attosecond X-ray pulses with gigawatt peak power from a free-electron laser. *Nat. Photon.* **14**, 30–36 (2020).
24. Popmintchev, T. et al. Phase matching of high harmonic generation in the soft and hard X-ray regions of the spectrum. *Proc. Natl Acad. Sci. USA* **106**, 10516–10521 (2009).
25. Li, K., Labeye, M., Ho, P. J., Gaarde, M. B. & Young, L. Resonant propagation of x rays from the linear to the nonlinear regime. *Phys. Rev. A* **102**, 053113 (2020).
26. Young, L. et al. Femtosecond electronic response of atoms to ultra-intense X-rays. *Nature* **466**, 56–61 (2010).
27. Kanter, E. P. et al. Unveiling and driving hidden resonances with high-fluence, high-intensity X-ray pulses. *Phys. Rev. Lett.* **107**, 233001 (2011).
28. Tanaka, S. & Mukamel, S. Coherent X-ray Raman spectroscopy: a nonlinear local probe for electronic excitations. *Phys. Rev. Lett.* **89**, 043001 (2002).
29. Gel'mukhanov, F. & Ågren, H. Resonant X-ray Raman scattering. *Phys. Rep.* **312**, 87–330 (1999).
30. Weninger, C. & Rohringer, N. Stimulated resonant X-ray Raman scattering with incoherent radiation. *Phys. Rev. A* **88**, 053421 (2013).
31. Kroll, T. et al. Observation of seeded Mn Kβ stimulated X-ray emission using two-color X-ray free-electron laser pulses. *Phys. Rev. Lett.* **125**, 037404 (2020).
32. Bergmann, U. Stimulated X-ray emission spectroscopy. *Photosynth. Res.* **162**, 371–384 (2024).
33. Bonifacio, R., De Salvo, L., Pierini, P., Piovella, N. & Pellegrini, C. Spectrum, temporal structure, and fluctuations in a high-gain free-electron laser starting from noise. *Phys. Rev. Lett.* **73**, 70–73 (1994).
34. Krinsky, S. & Gluckstern, R. L. Analysis of statistical correlations and intensity spiking in the self-amplified spontaneous-emission free-electron laser. *Phys. Rev. Accel. Beams* **6**, 050701 (2003).
35. Frasinski, L. J., Codling, K. & Hatherly, P. A. Covariance mapping: a correlation method applied to multiphoton multiple ionization. *Science* **246**, 1029–1031 (1989).
36. Kimberg, V. & Rohringer, N. Stochastic stimulated electronic X-ray Raman spectroscopy. *Struct. Dyn.* **3**, 034101 (2016).
37. Kayser, Y. et al. Core-level nonlinear spectroscopy triggered by stochastic X-ray pulses. *Nat. Commun.* **10**, 4761 (2019).
38. Driver, T. et al. Attosecond transient absorption spooktroscopy: a ghost imaging approach to ultrafast absorption spectroscopy. *Phys. Chem. Chem. Phys.* **22**, 2704–2712 (2020).
39. Zhaunerchyk, V., Frasinski, L., Eland, J. H. & Feifel, R. Theory and simulations of covariance mapping in multiple dimensions for data analysis in high-event-rate experiments. *Phys. Rev. A* **89**, 053418 (2014).
40. Müller, A. et al. Photoionization of Ne atoms and Ne+ ions near the K edge: precision spectroscopy and absolute cross-sections. *Astrophys. J.* **836**, 166 (2017).
41. Gel'mukhanov, F., Odelius, M., Polyutov, S. P., Föhlisch, A. & Kimberg, V. Dynamics of resonant X-ray and Auger scattering. *Rev. Mod. Phys.* **93**, 035001 (2021).
42. Liao, C.-T., Sandhu, A., Camp, S., Schafer, K. J. & Gaarde, M. B. Beyond the single-atom response in absorption line shapes: probing a dense, laser-dressed helium gas with attosecond pulse trains. *Phys. Rev. Lett.* **114**, 143002 (2015).
43. Vannucci, G. & Teich, M. C. Computer simulation of superposed coherent and chaotic radiation. *Appl. Opt.* **19**, 548–553 (1980).
44. Pfeifer, T., Jiang, Y., Düsterer, S., Moshammer, R. & Ullrich, J. Partial-coherence method to model experimental free-electron laser pulse statistics. *Opt. Lett.* **35**, 3441–3443 (2010).
45. Li, K. et al. Ghost-imaging-enhanced noninvasive spectral characterization of stochastic X-ray free-electron-laser pulses. *Commun. Phys.* **5**, 191 (2022).
46. Weninger, C. & Rohringer, N. Transient-gain photoionization X-ray laser. *Phys. Rev. A* **90**, 063828 (2014).
47. Lutman, A. et al. Femtosecond X-ray free electron laser pulse duration measurement from spectral correlation function. *Phys. Rev. Accel. Beams* **15**, 030705 (2012).
48. Miyawaki, J. et al. Design of ultrahigh energy resolution RIXS beamline at NanoTerasu. *J. Phys. Conf. Ser.* **2380**, 012030 (2022).
49. Betzig, E. et al. Imaging intracellular fluorescent proteins at nanometer resolution. *Science* **313**, 1642–1645 (2006).
50. Higley, D. J. et al. Stimulated resonant inelastic X-ray scattering in a solid. *Commun. Phys.* **5**, 83 (2022).
51. Alexander, O. et al. Attosecond impulsive stimulated X-ray Raman scattering in liquid water. *Sci. Adv.* **10**, eadp0841 (2024).
52. Cavaletto, S. M., Keefer, D. & Mukamel, S. High temporal and spectral resolution of stimulated X-ray Raman signals with stochastic free-electron-laser pulses. *Phys. Rev. X* **11**, 011029 (2021).

Methods

Characterization of SASE structure

Measured and simulated spike distribution. To simulate the XFEL pulses, the SASE spectra are examined to obtain statistical characteristics of the distribution of spikes in each pulse. A representative single-shot spectrum is shown in Extended Data Fig. 1a. The peaks of the spikes from 1,000 shots are identified, and the distribution of energy spacings (ΔE) between adjacent spikes is shown in Extended Data Fig. 1b. The spacing ranges from 0.2 eV up to 1.5 eV, with a maximum at around 0.5 eV. The number of spikes in each pulse varies from 18 to 30, with most of the shots containing approximately 23 spikes. The averaged spectral bandwidth is 7.5 eV (FWHM), and the pulse duration is estimated to be around 40 fs (FWHM) using the method in ref. 47.

The partial-coherence method[43,44] can be used to model the SASE pulse. In this method, the averaged photon energy spectrum is assumed to be a Gaussian function centred at 867.5 eV with an FWHM of 7.5 eV. The initial spectral intensity at a specific photon energy is sampled from a normal distribution that has a standard deviation equal to the average spectral intensity at that photon energy. The initial phase at each photon energy is assumed to fluctuate randomly within the range of $-\pi$ to π. There are 2^{13} spectral points with spacing $\Delta f = 1/300$ fs. The initial temporal profile of the pulse is obtained by a Fourier transform of the initial spectrum. As the spectral phase is initially random, the resulting field spans the whole time window of 300 fs. The Gaussian spectral intensity profile generates temporal coherent spikes with an FWHM of around 0.25 fs (0.44/7.5 eV, that is, the Fourier transform limit). To ensure the average pulse duration is 40 fs, a Gaussian mask function with a duration of 40 fs (FWHM) is applied to the pulse in the time domain. An example of the simulated single-shot temporal profile is shown in Extended Data Fig. 1j. Afterwards, an inverse Fourier transform is applied to obtain the final spectrum as shown in Extended Data Fig. 1d. The final spectrum contains coherent spikes with an FWHM of around 0.1 eV (1/40 fs). The corresponding statistical analysis of the spike spacing and number of spikes per pulse is shown in different panels of Extended Data Fig. 1. It is noted that the measured spectra are broadened by the 0.2-eV spectrometer resolution, and the simulated spectrum convolved with a 0.2-eV Gaussian function matches the measured spectrum.

Measured and simulated spectral spike intensity fluctuation. The fluctuation of the SASE spectra from shot to shot is the basis of covariance analysis. In Extended Data Fig. 2, we present the percentage fluctuation of both the measured (Extended Data Fig. 2a) and the simulated (Extended Data Fig. 2b) spectra with respect to their average. The SASE spectra, with central photon energy at around 867.5 eV, were recorded with an empty gas cell. The averaged spectrum exhibits a skewed Gaussian shape, with a bandwidth of 7.5 eV (FWHM) and longer tails at higher photon energies. The single-shot spectrum displays fluctuations in the form of spikes that vary from shot to shot. To quantify these fluctuations, we calculated the standard deviation (STD) of the signal at different photon energies and expressed it as a percentage of the mean value (STD/mean). The percentage fluctuation shows a minimum value of 33% around 867 eV and increases on both sides as the energy detunes from the centre. The curve exhibits a marked increase at both edges because of the relatively weak signals in those regions.

Extended Data Figure 2b shows the simulated spectrum, which exhibits more spikes compared with the measured spectrum. The average of the simulated spectra resembles a Gaussian function with an FWHM of 7.5 eV, consistent with the measured SASE pulse. However, owing to the fully random fluctuation of the spikes from shot to shot, the percentage fluctuation remains steady at around 100%.

Detector calibration for XRS + XRL yield

The pulse energy of stimulated XRS and XRL can be estimated by calibrating the detection system after the gas cell. In our experiment, we scanned the gas attenuator[53] to adjust the incident pulse energy at 850 eV in the absence of gas. To prevent detector saturation, we switch between three filters with thicknesses of 3.5 μm, 5 μm and 10 μm. After dividing the transmission of the filters, the spectra detected are presented in Extended Data Fig. 3a. Before reaching the experimental endstation, the XFEL pulse energy is measured using a gas monitor detector. The pulse energy incident on the gas cell is then estimated by multiplying the measured energy by the beamline transmission of about 0.5. The calibration between the integrated spectra and pulse energy is fitted using a linear function, which is shown in Extended Data Fig. 3b. By applying this calibration function, we estimated the pulse energy of the emission from a 2-bar neon gas with full XFEL intensity is 0.06 mJ, corresponding to 4.4×10^{11} photons at 849 eV.

An alternative approach for estimating the XRS + XRL yield is using the experimental geometry (Extended Data Fig. 4). The X-rays generated from the undulators are focused to a spot size of 1–2 μm (FWHM) on a gas cell using Kirkpatrick–Baez mirrors[54]. The X-ray emitted and transmitted through the gas cell is approximately 0.4 mrad. It passes through an aluminium filter and a slit and is then reflected by a grating before being detected by a soft X-ray Andor detector with 2,048 × 512 active pixels and a 13.5 × 13.5 μm pixel size. Three filters with 3.5 μm, 5 μm and 10 μm are mounted on a translatable frame, and their transmission (T_{filter}) at 850 eV is estimated to be 0.173, 0.081 and 0.006, respectively[55]. The footprint of the X-ray beam on the slit, which has an opening of approximately 10 μm, is around 1 mm at a distance of 1.4 m downstream. Around $T_{\text{slit}} = 1\%$ of the X-rays passing through the slit are dispersed by the grating with approximately $R_{\text{grating}} = 1\%$ at a high-order reflection. The non-dispersive direction of the detector is set to 64 bins to obtain a data acquisition rate of 10 Hz. The detected photon number can be estimated by

$$N_{\text{ph}} = \frac{N_{\text{count}}/(E_{\text{ph}}\,[\text{eV}]/3.65\,[\text{eV per count}])/Q}{T_{\text{filter}} \times T_{\text{slit}} \times R_{\text{grating}}}$$

where $Q \approx 0.8$ is the quantum efficiency of the detector. Roughly 850 eV/3.65 eV per count = 233 photoelectrons are generated with each detected X-ray photon at 850 eV. The high-sensitivity mode of the detector is used to register one count per photoelectron. With 10 μm filter and 2 bar neon gas, the average registered counts of SRS and XRL per XFEL pulse are around 5×10^6. Given the efficiency and transmission of the upstream elements mentioned above, the estimated photon number of SRS and XRL is around 5×10^{10}. This rough estimate is consistent with our previous calibration.

Super-resolution s-SXRS resolution

Spectrometer resolution. The instrumental broadening of the spectrometer can be determined by fitting the absorption spectrum of the Ne $1s \rightarrow 3p$ transition (Extended Data Fig. 5). To avoid nonlinear effects, we set the gas attenuator to 1% transmission and the target neon gas pressure to 0.06 bar. Around 1,800 single-shot spectra were recorded, and the measured XAS was calculated as $-\ln(I(\omega)/I_0(\omega))$, where $I(\omega)$ is the averaged spectrum with neon gas and $I_0(\omega)$ is the averaged spectrum without neon gas. The experimental XAS result is fitted with a Voigt profile, which is a Gaussian profile convolved with a Lorentzian profile. The optimized fitting gives central photon energy at 867.3 eV, with a Gaussian function FWHM of 0.18 eV and a Lorentzian function FWHM of 0.27 eV. The Lorentzian FWHM matches with the neon 1*s* excited state lifetime broadening in the literature. The Gaussian broadening is assigned to the spectrometer instrumental broadening.

Pixel-size-limited super-resolution s-SXRS. Super-resolution s-SXRS is obtained by calculating the normalized partial covariance using peak-position localized single-shot spectra. The spectral resolution is determined by the localization precision δ_l instead of the instrumental broadening and the SASE spike bandwidth. As known from super-resolution microscopy, the peak localization uncertainty is $\delta_m/\sqrt{N}$, where δ_m is the original measurement resolution—that is, the diffraction limit—and N is the number of photons collected for each molecular localization. For our spectral localization, δ_m is the FWHM of the original measured spectral spikes, which is a convolution of SASE spike $\sigma_s \approx 0.1$ eV and the spectrometer instrumental broadening $\sigma_0 \approx 0.18$ eV, that is, $\delta_m = \sqrt{\sigma_s^2 + \sigma_0^2} = 0.2$ eV. The number of photons collected for each spectral spike N can be estimated by dividing the total number of photons in the XRS emission spectral band by the number of spikes. As shown above in the detector calibration section, the total counts in the XRS and XRL regions is around 5×10^6. Each 850 eV photon generates 233 counts; this gives an estimation of the number of emission photons on the detector to be around 20,000. With an average of 30 SASE spikes in each pulse, the photons per spike are $N \sim 600$. Owing to our simple localization method, which only keeps the peak values and discards the others, the localization resolution cannot exceed the pixel size limitation $\delta_p = 0.055$ eV, as obtained from spectrometer calibration. Thus, ideally, the spectral localization uncertainty is $\delta_l = \sqrt{\left(\frac{\delta_m}{\sqrt{N}}\right)^2 + (\delta_p)^2} \approx 0.056$ eV. Considering the localization uncertainty is the same for all the spectra, and it already contains both the SASE spike and spectrometer broadening before localization, using the s-SXRS resolution equation derived in Supplementary Information section III, we get the super-resolution s-SXRS resolution $\sigma = \sqrt{2(\delta_l)^2} \approx 0.079$ eV. This confirms that, in our experiment, the main limitation of the resolution of the super-resolution s-SXRS is the detector pixel size.

The super-resolution s-SXRS linewidth can be smaller than 0.1 eV, that is, the SASE spike limitation associated with the 40-fs pulse duration. The quoted 0.1-eV linewidth was obtained from a Gaussian function fit of the energy-loss projected spectrum. However, the dispersive s-SXRS line is distorted around resonance because of the interplay of the 1*s* excited state lifetime broadening and the incident SASE spike bandwidth. By fitting the super-resolution s-SXRS in a non-distorted background-free regime, better resolution can be obtained. This is shown in Extended Data Fig. 6a, in which Gaussian profile fitting is applied to 10 lineouts of the super-resolution s-SXRS with 1 bar neon gas within the range $\omega_1 \in [866.1, 866.8]$ eV. The fitting results are shown in Extended Data Fig. 6b, with the Gaussian FWHM divided by $\sqrt{2}$ to obtain the expected energy-loss axis projected resolution. The resolution can be smaller than the 0.1 eV SASE spike bandwidth, and several FWHMs are about 0.08 eV, once again confirming that the super-resolution s-SXRS resolution limitation is set by the pixel size and not by SASE spike width or the spectrometer resolution.

Data availability

The experimental data were collected during beamtime 2748 at the European XFEL. The raw and metadata are available at https://in.xfel.eu/metadata/doi/10.22003/XFEL.EU-DATA-002748-00. The experimental and simulation datasets used in the figures are deposited at Zenodo[56] (https://doi.org/10.5281/zenodo.15253560).

Code availability

The code used for the propagation simulations is available from K.L. or M.B.G. upon reasonable request.

53. Dommach, M. et al. The photon beamline vacuum system of the European XFEL. *J. Synchrotron Radiat.* **28**, 1229–1236 (2021).
54. Mazza, T. et al. The beam transport system for the small quantum systems instrument at the European XFEL: optical layout and first commissioning results. *J. Synchrotron Radiat.* **30**, 457–467 (2023).
55. Henke, B. L., Gullikson, E. M. & Davis, J. C. X-ray interactions: photoabsorption, scattering, transmission, and reflection at E = 50-30,000 eV, Z = 1-92. *At. Data Nucl. Data Tables* **54**, 181–342 (1993).
56. Li, K. Super-resolution stimulated X-ray Raman spectroscopy. *Zenodo* https://doi.org/10.5281/zenodo.15253560 (2025).
57. Nordgren, J. et al. Soft X-ray emission spectroscopy using monochromatized synchrotron radiation. *Rev. Sci. Instrum.* **60**, 1690–1696 (1989).

Acknowledgements We thank C. Knight for assistance with porting the TDSE-MWE code to the Argonne Leadership Computing Facility and S. H. Southworth and J. Rouxel for their discussions. We thank N. Rohringer for providing the detector for the experiment. This work was primarily supported by the US Department of Energy, Office of Science, Basic Energy Science, Chemical Sciences, Geosciences and Biosciences Division under contract no. DE-AC02-06CH11357, which also supported M.G. under contract no. DE-SC0010431. M.M. acknowledges support by the Cluster of Excellence 'Advanced Imaging of Matter' of the DFG–EXC 2056 and project ID 390715994. T.P. acknowledges support by the Deutsche Forschungsgemeinschaft (DFG, German Research Foundation) under Germany's Excellence Strategy EXC2181/ 1–390900948 (the Heidelberg STRUCTURES Excellence Cluster) and by the European Research Council (ERC) (X-MuSiC 616783). We acknowledge the European XFEL in Schenefeld, Germany, for beam time at the SQS endstation under proposal no. 2748 and would like to thank the staff for their assistance.

Author contributions K.L. and L.Y. conceptualized the stochastic stimulated X-ray Raman study. C.O., A.M., T.P., J.-E.R., M.A., M.M., K.L., G.D. and L.Y. planned and designed the experimental layout. C.O., A.M., M.R., M.A., J.-E.R., N.R. and T.M. set up the experimental configuration and performed data collection together with K.L., G.D., M.S., M.M., A.D.F., T.M.B., J.M., S.U., Y.O., T.P. and L.Y.; K.L. and K.C. performed simulations with P.J.H. and M.B.G.; K.L. performed data analysis and interpretation with M.B.G., T.P., J.-E.R. and L.Y.; L.C. provided CCSD electronic structure calculations. T.P. suggested the super-resolution method. K.L. and L.Y. wrote the paper with inputs from all authors.

Competing interests The authors declare no competing interests.

Additional information

Supplementary information The online version contains supplementary material available at https://doi.org/10.1038/s41586-025-09214-5.

Correspondence and requests for materials should be addressed to Kai Li, Thomas Pfeifer or Linda Young.

Peer review information *Nature* thanks Mizuho Fushitani, Victor Kimberg and the other, anonymous, reviewer(s) for their contribution to the peer review of this work. Peer reviewer reports are available.

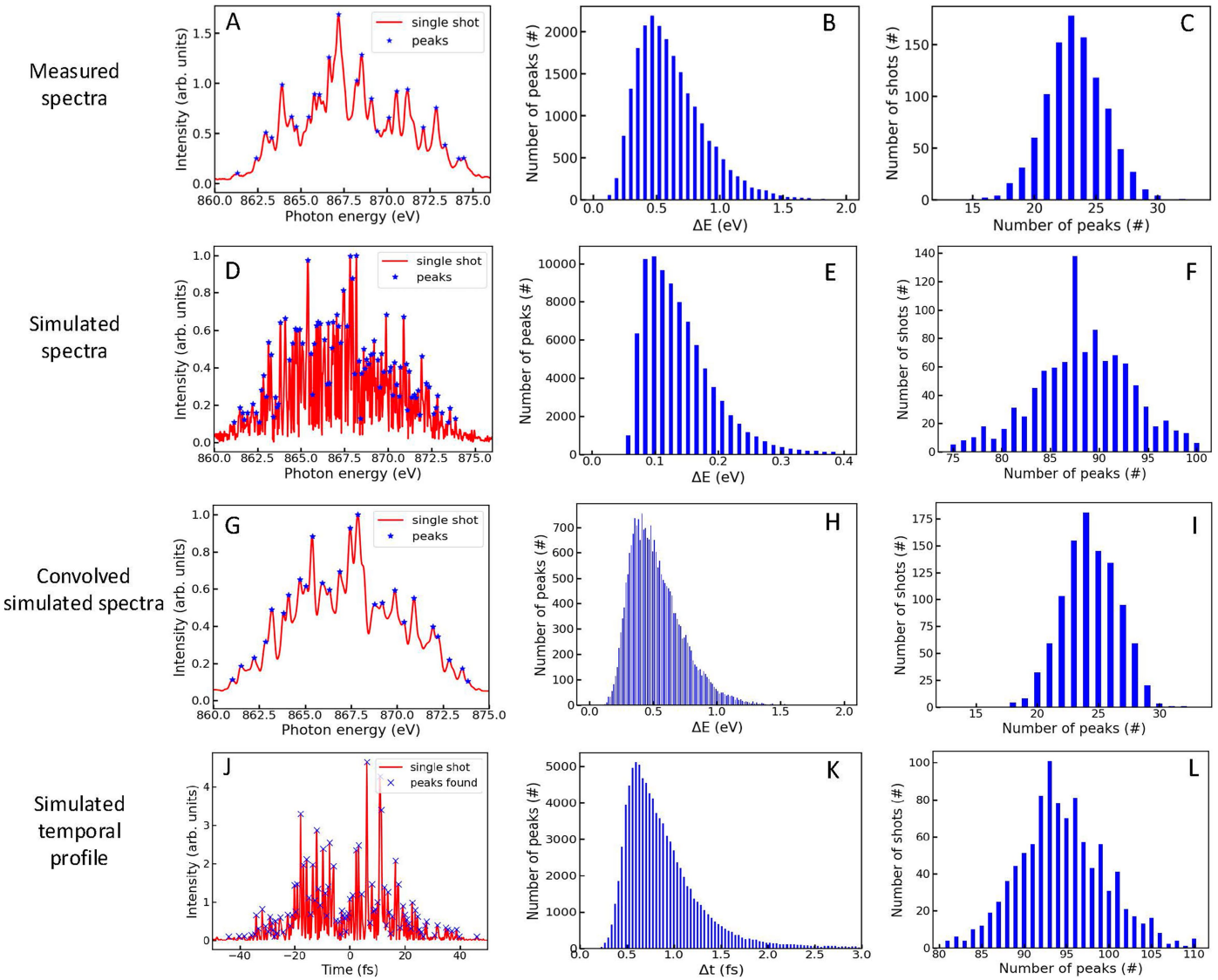

Extended Data Fig. 1 | Measured vs simulated spike distribution. Spike analysis of measured (first row) and simulated (lower rows) SASE spectra. (A) a randomly selected single-shot spectrum normalized to the peak intensity of the averaged spectra. The peaks are identified with adjacent spacing larger than 0.1 eV and height above 0.1. The statistics of the spacing between adjacent spikes (B) and the number of peaks per shot (C) are obtained by analyzing 1000 shots. The maximum of distribution of spacing between adjacent spikes is around 0.5 eV, and most of the shots have approximately 23 spikes. The corresponding analyses of the simulated SASE are shown in the lower panels. The distribution curves and spectra look similar, but there are more spikes (90) in the simulated SASE, and the distribution of the spacing between the spikes peaks at around 0.1 eV. The difference is due to the 0.2 eV spectrometer broadening of the measured SASE pulse. The simulated spectra and statistics are close to the experimental results after convolving with a 0.2 eV Gaussian function (G). A representative simulated single-shot temporal profile is shown in (J). The statistics of the temporal profile of 1000 shots show a most likely adjacent spike spacing of 0.6 fs with 93 temporal spikes in a pulse.

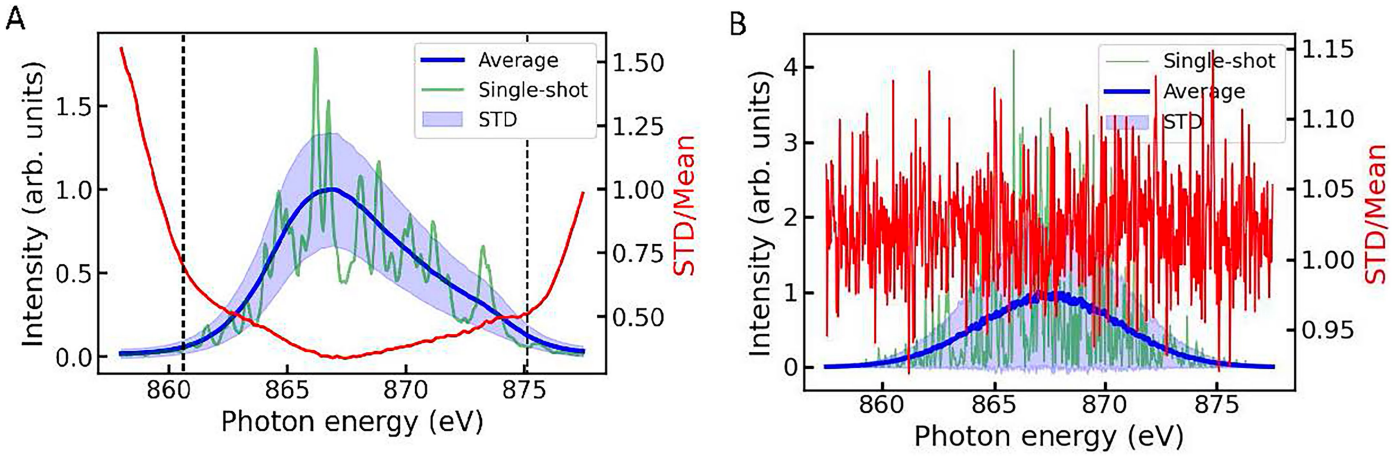

Extended Data Fig. 2 | Measured vs simulated spectral spike intensity fluctuation. (A) Single-shot SASE spectra were measured as the gas cell was empty. The spikes in the pulse exhibit random fluctuations from shot to shot. The average spectrum displays a smooth Gaussian profile with a 7.5 eV bandwidth (FWHM). The standard deviation (std) of the spectral intensity fluctuation at a fixed photon energy is calculated, and the resulting percentage fluctuation (std/mean) remains steady at approximately 40% within the main spectrum. (B) The average simulated spectrum also exhibits a Gaussian profile with a 7.5 eV bandwidth (FWHM). However, it contains more spikes that fluctuate fully randomly from shot to shot, resulting in a steady 100% fluctuation of the intensity across the entire spectrum.

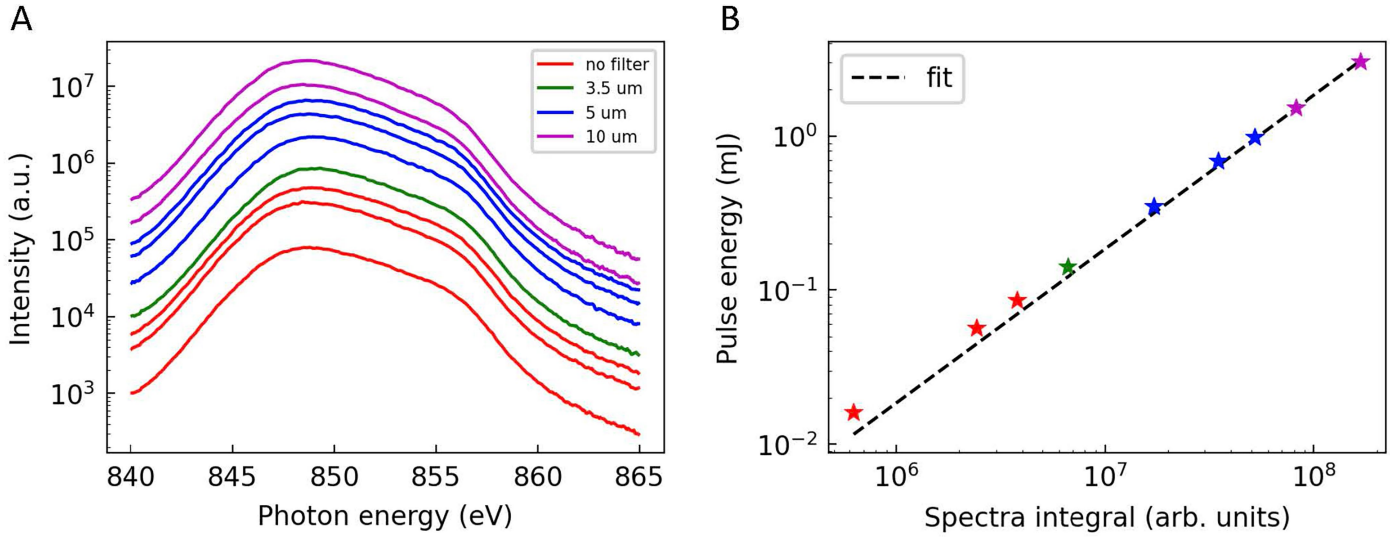

Extended Data Fig. 3 | Detector Cailbration. (A) Calibration of the detection system using spectra integral to pulse energy. The SASE pulses with a center photon energy of 850 eV pass through an empty gas cell, and the GATT and filters are adjusted to optimize the signals on the detector. Three filters with thicknesses of 3.5, 5, and 10 μm are employed, and their attenuation is divided to obtain the spectra. (B) The incident pulse energy is obtained by multiplying the energy measured by an upstream gas monitor detector with the beamline transmission factor of approximately 0.5. The linear relationship between integrated spectra intensity and incident pulse energy provides a calibration that can be used to estimate the pulse energy emitted for subsequent runs with the gas in the cell.

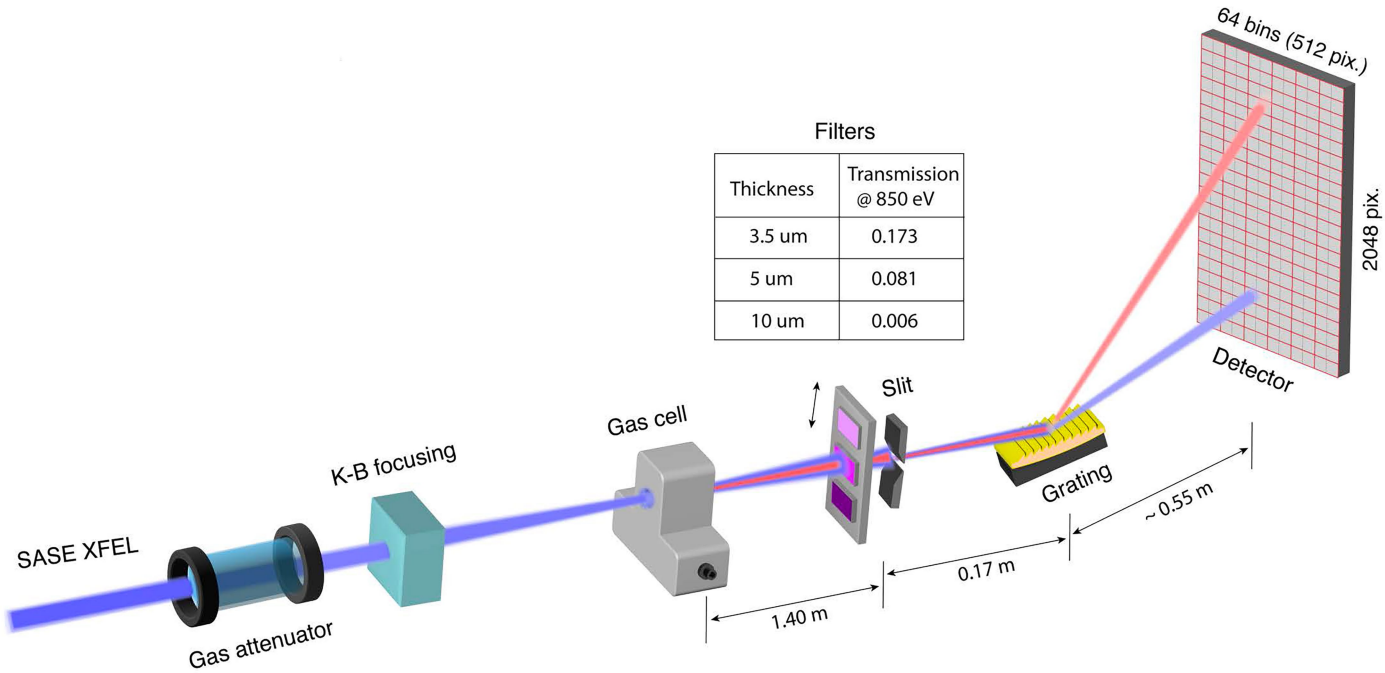

Extended Data Fig. 4 | Experimental Setup. The XFEL pulses are focused on a gas cell by K-B mirrors. The transmitted and emitted x rays pass through an Al filter and a slit before being dispersed on the pixelated Andor detector by a spherical grating with 5-m radius and 1200 lines/mm[57].

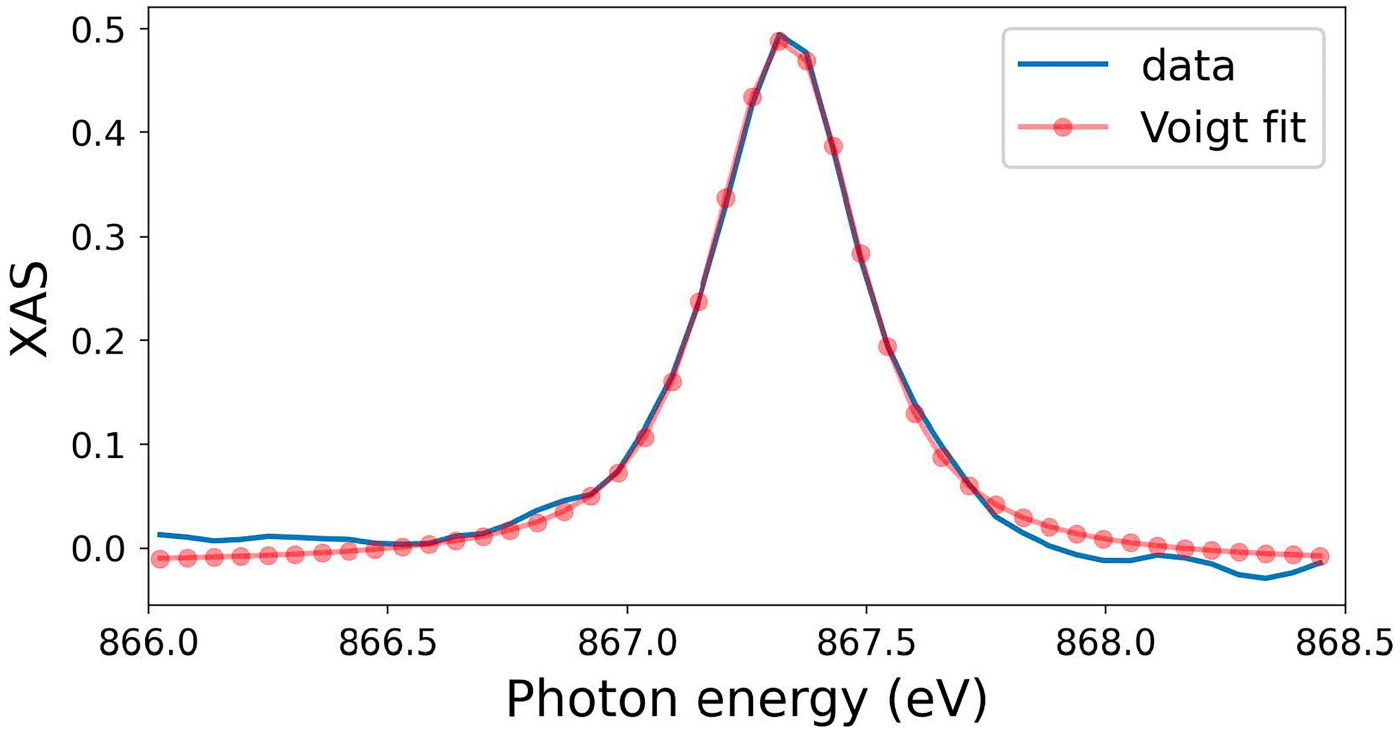

Extended Data Fig. 5 | Spectrometer resolution. The XAS of neon $1s \rightarrow 3p$ transition with GATT=0.01 and gas pressure 0.06 bar. The absorption spectrum is fitted by Voigt function. The optimum fitting obtained has center photon energy 867.3 eV, Gaussian FWHM 0.18 eV, and Lorentzian FWHM 0.27 eV.

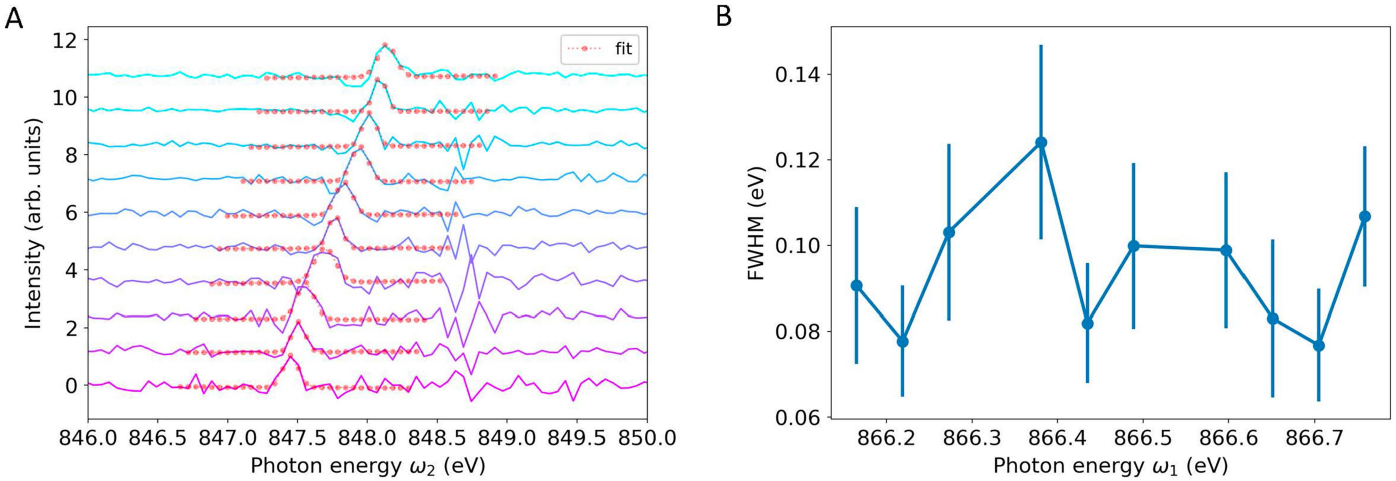

Extended Data Fig. 6 | Pixel-limited super-resolution. The super-resolution s-SXRS has linewidth smaller than the SASE spike bandwidth 0.1 eV when fitting at regions away from the resonances that are distorted. (A) The Gaussian fitting of the 10 lineouts of the super-resolution s-SXRS with 1.0 bar neon pressure (2D map shown in the main text) in the range $\omega_1 \in [866.1, 866.8]$ eV. (B) The FWHM of the fitted Gaussian functions at different ω_1 lineouts. The FWHM data is divided by $\sqrt{2}$ to show the expected energy-loss axis projected resolution.